First-principles study of the drift and Hall mobilities of perovskite $BaSnO_3$

Jinlong Ma,[1,*] Wu Li,[2] and Xiaobing Luo[1]
[1]*School of Energy and Power Engineering, Huazhong University of Science and Technology, Wuhan 430074, China*
[2]*Institute for Advanced Study, Shenzhen University, Shenzhen 518060, China*

(Received 11 April 2022; revised 16 June 2022; accepted 30 June 2022; published 11 July 2022)

Barium stannate ($BaSnO_3$) is an emerging perovskite oxide with promising properties for many potential applications. One of the most outstanding properties is the high-room-temperature electron mobility. The extraordinary superior electronic transport performance has attracted great attention but the research is limited by semiempirical assumptions. In this work, the first-principles calculations are employed to study the electronic transport of $BaSnO_3$ by solving the Boltzmann transport equation (BTE) with full information on electron, phonon, and electron-phonon interactions taken into account. The mode-resolved analyses of scattering rates show that the longitudinal optical (LO) phonons dominate the scattering processes not only at low but also at high carrier concentrations. As a consequence, the energy relaxation time approximation significantly underestimates the solution of BTE due to the divergent coupling coefficient of electrons and LO phonons. The drift and Hall mobilities are calculated in the framework of BTE in the presence of electric and magnetic fields. At low concentration limits, the room-temperature drift and Hall mobilities are 357 and 418 $cm^2\,V^{-1}\,s^{-1}$, respectively, while the Hall factor is temperature dependent with values between 1.06 and 1.17 in the temperature range of 100 K to 800 K. In the doping system with carrier concentration above 1×10^{19} cm^{-3}, the upper limit of drift mobility is 377 $cm^2\,V^{-1}\,s^{-1}$ at room temperature, and the Hall factor becomes smaller than 1, which cannot be revealed by the formula under the isotropic parabolic assumption at all, indicating the importance of magnetic transport calculation from *ab initio* based BTE.

DOI: 10.1103/PhysRevB.106.045201

I. INTRODUCTION

Perovskite oxides are types of important functional materials with great application potential due to their diverse compositions and thus providing a rich variety of outstanding physical properties. Nevertheless, the carrier mobilities of most perovskite oxides are usually not good above room temperature [1–4], limiting their technological applications that must combine high carrier conductivity at low carrier concentrations. Barium stannate ($BaSnO_3$) has recently attracted considerable attention especially after the discovery of its high-room-temperature mobility, which is the highest value among the reported perovskite oxides. The early experiments realized the synthesization of *n*-type $BaSnO_3$ epitaxial films by doping La in place of Ba or Sb in place of Ba, but the films show minuscule mobility at room temperature [5,6]. Taking the strategy of La doping, Luo *et al.* [7] have grown single-crystal $BaSnO_3$ to the bulk regime, and discovered a room-temperature mobility as large as 103 $cm^2\,V^{-1}\,s^{-1}$ under *n*-type carrier concentrations of 8–10 $\times$ 10^{19} cm^{-3}. Immediately following, Kim *et al.* [8,9] obtained a much higher value of up to 300 $cm^2\,V^{-1}\,s^{-1}$ at a concentration of 8×10^{19} cm^{-3}. This value is higher than the mobilities under a similar doping level in the wide-band-gap oxide semiconductors of current commercial devices [10,11]. Thus, great interest has arisen in understanding the fundamentals of the high-room-temperature mobility of $BaSnO_3$.

The small electron effective mass around the conduction band edge, originating from the antibonding *s* state of the Sn-O hybridization [12], is suggested as the primary source of the high mobility [8]. Moreover, the size of the La atom is similar to that of the Ba atom with a valence difference of only 1 and the La ion doped at the Ba site is away from the SnO_6 octahedron inside the unit cell; as a result, the disorder due to La doping is not strong [8]. The significantly lower scattering rates than other perovskite oxides also have an important role in yielding the high mobility from the numerical analysis [13], but therein, the pivotal electron-phonon (el-ph) scattering is only derived from longitudinal optical (LO) phonons at three fixed frequencies by premising that the Coulomb interaction is strong enough so that the LO phonons tend to dominate the scattering as compared to other phonons. However, the plausibility of such an assumption needs further verification, because even for the most representative strong-polarity GaAs, the dominance of LO phonon scattering does not always hold especially at high temperatures and high carrier concentrations where the contribution from high-energy carriers increases [14,15]. Therefore, it is urgent to investigate the el-ph scattering mechanisms involving full phonon modes.

The method taking account of full el-ph scattering has been realized based on solving the mode-resolved Boltzmann transport equation (BTE) [16,17], in which the el-ph coupling strength in each electron and phonon pair is obtained from the density functional theory (DFT) and density functional

*majinlong@hust.edu.cn

perturbation theory (DFPT) calculations. In practical implementation, an interpolation scheme based on the Wannier function transformation [18] is generally used to accelerate the computations especially for the heavy el-ph coupling matrix. Since the Wannier basis is a localized representation, a correction accounting for the long-range Fröhlich interaction is additionally employed [19,20]. This *ab initio* approach has been successfully applied to many polar materials of current interest [14–16,21–28]. The calculation processes do not resort to empirical parameters, and thus this approach has predictive accuracy which is a favorable choice to analyze the electronic transport.

Specifically for $BaSnO_3$, generally considered as a cubic crystal structure with space group of $Pm\bar{3}m$, there is a problem that the calculated phonon dispersion has imaginary modes in the DFT and DFPT calculations using Quantum ESPRESSO (QE) [29] with many different types of pseudopotentials [12,30]. In the literature, to sum up, the imaginary phonon frequency is eliminated in two cases of calculations. One is based on the DFPT calculations using antiquated norm-conserving pseudopotentials with the 4*d* states of Sn or 5*s* and 5*p* states of Ba frozen in the core [31–33], but the calculated phonon frequencies deviate greatly from the experiments. The other one is performing finite-difference supercell calculations using the Vienna *Ab initio* Simulation Package (VASP) with projector augmented wave (PAW) pseudopotentials and the HSE hybrid exchange-correlation functional [34,35], which gives good agreement with experiments in lattice constant and phonon dispersion. It has been demonstrated by experiments that $BaSnO_3$ remains a perfectly cubic crystal structure down to 10 K [33]. Therefore, in this work, we take the calculations for cubic $BaSnO_3$, and the phonon dispersion without imaginary modes is obtained from VASP with HSE pseudopotentials.

In common practice, the mobility is measured from Hall experiments where the electric and magnetic fields exist simultaneously. The measured mobility is called the Hall mobility, whereas the mobility under pure electric field is known as drift mobility. Therefore, involving the influence of magnetic field in the calculations is more justified for the comparison with the experiments. There have been early attempts to calculate the magnetotransport but based on many parametrizations and simplifications [36–39]. Very recently, expanding the current first-principles framework of electric transport, the parameter-free calculation of magnetic transport has been achieved by solving the linearized BTE in the presence of both electric field and magnetic field [40,41]. The calculated magnetotransport coefficients are in good agreement with experiments. In this work, employing this *ab initio* approach, the Hall and drift mobilities of $BaSnO_3$ are calculated, and the Hall factor is found to be temperature and concentration dependent. The phonon-limited scattering mechanisms are analyzed at different carrier concentrations, showing that the LO phonon scattering is dominant.

II. METHODOLOGY

The kernel for computing charge carrier transport is the el-ph coupling element $g_{nm\nu}(\mathbf{k},\mathbf{q})$, which measures the probability of electron scattering from an initial state $|\psi_{n\mathbf{k}}\rangle$ to a final state $|\psi_{m\mathbf{k+q}}\rangle$ by absorbing and emitting a phonon mode $\mathbf{q}\nu$. The $\mathbf{k}$ and $\mathbf{q}$ are the electron and phonon momenta in reciprocal space, respectively, while $n(m)$ and ν denote the corresponding band and mode indices. The phonon energy $\hbar\omega_{\mathbf{q}\nu}$ and eigenvector $\mathbf{e}_{\mathbf{q}\nu}$ are also involved, written as [16,17]

$$g_{nm\nu}(\mathbf{k},\mathbf{q}) = \sqrt{\frac{\hbar}{2\omega_{\mathbf{q}\nu}}} \sum_{ls\alpha} \frac{\mathbf{e}_{\mathbf{q}\nu}}{\sqrt{M_s}} \langle \psi_{m\mathbf{k+q}} | \partial_{\mathbf{q}s\alpha} V | \psi_{n\mathbf{k}} \rangle, \quad (1)$$

where $\partial_{\mathbf{q}s\alpha}V$ is the change of potential due to lattice displacement of atom s in the lth unit cell along the α direction. The el-ph coupling matrix determines the phonon-limited transition probability $W^{\mathbf{q}\nu}_{n\mathbf{k},m\mathbf{k+q}}$ including phonon absorption and emission processes as

$$\begin{aligned} W^{\mathbf{q}\nu}_{n\mathbf{k},m\mathbf{k+q}} = {} & \frac{2\pi}{\hbar} |g_{nm\nu}(\mathbf{k},\mathbf{q})|^2 \\ & \times \left[\left(n^0_{\mathbf{q}\nu} + f^0_{m\mathbf{k+q}}\right) \delta(\varepsilon_{n\mathbf{k}} + \hbar\omega_{\mathbf{q}\nu} - \varepsilon_{m\mathbf{k+q}}) \right. \\ & \left. + \left(1 + n^0_{\mathbf{q}\nu} - f^0_{m\mathbf{k+q}}\right) \delta(\varepsilon_{n\mathbf{k}} - \hbar\omega_{\mathbf{q}p} - \varepsilon_{m\mathbf{k+q}}) \right], \end{aligned} \quad (2)$$

where $\varepsilon_{n\mathbf{k}}$ is the electronic energy, and $f^0_{n\mathbf{k}}$ and $n^0_{\mathbf{q}\nu}$ are the electron and phonon equilibrium occupations given by the Fermi-Dirac distribution and Bose-Einstein distribution, respectively.

At steady state, the BTE with small electric field ($\mathbf{E}$) and magnetic field ($\mathbf{B}$) is [40,41]

$$\begin{aligned} & -e\frac{\partial f^0_{n\mathbf{k}}}{\partial \varepsilon_{n\mathbf{k}}} \mathbf{v}_{n\mathbf{k}} \cdot \mathbf{E} + \frac{e}{\hbar}(\mathbf{v}_{n\mathbf{k}} \times \mathbf{B}) \cdot \nabla_{\mathbf{k}} f_{n\mathbf{k}} \\ & = \frac{1}{k_B T N_{\mathbf{q}}} \sum_{m\mathbf{q}\nu} f^0_{n\mathbf{k}}\left(1 - f^0_{n\mathbf{k}}\right) W^{\mathbf{q}\nu}_{n\mathbf{k},m\mathbf{k+q}} (\chi_{n\mathbf{k}} - \chi_{m\mathbf{k+q}}), \end{aligned} \quad (3)$$

where e is the electronic charge, $\hbar$ is the reduced Plank constant, $\mathbf{v}_{n\mathbf{k}}$ is the electronic velocity, $N_{\mathbf{q}}$ is the number of $\mathbf{q}$ points in the summation for phonon scattering, $f_{n\mathbf{k}}$ is the electronic distribution, and $\chi_{n\mathbf{k}}$ is a small perturbation related to the expansion of the distribution function as $f_{n\mathbf{k}} = f^0_{n\mathbf{k}} - \frac{\partial f^0_{n\mathbf{k}}}{\partial \varepsilon_{n\mathbf{k}}} \chi_{n\mathbf{k}}$. If writing $\chi_{n\mathbf{k}} = e\mathbf{E} \cdot \mathbf{F}_{n\mathbf{k}}$ and considering only the leading term, the linearized BTE is obtained as

$$\begin{aligned} & \mathbf{v}_{n\mathbf{k}} + \frac{e}{\hbar}(\mathbf{v}_{n\mathbf{k}} \times \mathbf{B}) \cdot \nabla_{\mathbf{k}} \mathbf{F}_{n\mathbf{k}} \\ & = \frac{1}{N_{\mathbf{q}}} \sum_{m\mathbf{q}\nu} W^{\mathbf{q}\nu}_{n\mathbf{k},m\mathbf{k+q}} (\mathbf{F}_{n\mathbf{k}} - \mathbf{F}_{m\mathbf{k+q}}). \end{aligned} \quad (4)$$

To solve $\mathbf{F}_{n\mathbf{k}}$ which implicitly depends on $\mathbf{B}$, the linearized BTE is reorganized in an iterative form given by [41]

$$\begin{aligned} \mathbf{F}^{i+1}_{n\mathbf{k}} = {} & \tau_{n\mathbf{k}} \mathbf{v}_{n\mathbf{k}} + \frac{\tau_{n\mathbf{k}}}{N_{\mathbf{q}}} \sum_{m\mathbf{q}\nu} W^{\mathbf{q}\nu}_{n\mathbf{k},m\mathbf{k+q}} \mathbf{F}^i_{m\mathbf{k+q}} \\ & + \tau_{n\mathbf{k}} \frac{e}{\hbar}(\mathbf{v}_{n\mathbf{k}} \times \mathbf{B}) \cdot \nabla_{\mathbf{k}} \mathbf{F}^i_{n\mathbf{k}}, \end{aligned} \quad (5)$$

where $\tau_{n\mathbf{k}}$ denotes the relaxation time computed as the inverse of scattering rate $\tau^{-1}_{n\mathbf{k}} = \frac{1}{N_{\mathbf{q}}} \sum_{m\mathbf{q}\nu} W^{\mathbf{q}\nu}_{n\mathbf{k},m\mathbf{k+q}}$. If the summation term on the right side is neglected, it is the energy relaxation time approximation (ERTA). When the transition probability is multiplied by a factor of $1 - \mathbf{v}_{m\mathbf{k+q}}\mathbf{v}_{n\mathbf{k}}/|\mathbf{v}_{n\mathbf{k}}|^2$, it is called

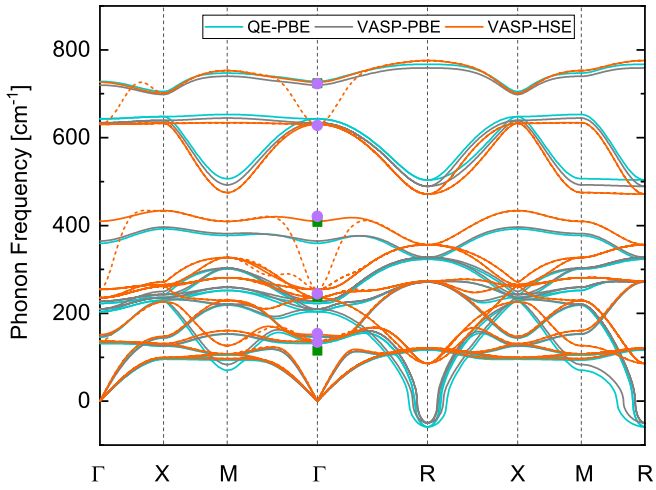

FIG. 1. Phonon dispersion of $BaSnO_3$ calculated using QE and VASP with PBE and HSE exchange-correlation functionals, compared with the experimental values measured by far-infrared (purple circles) and Raman (green squares) methods. The dashed lines are the phonon dispersion with dipole-dipole interactions removed [32].

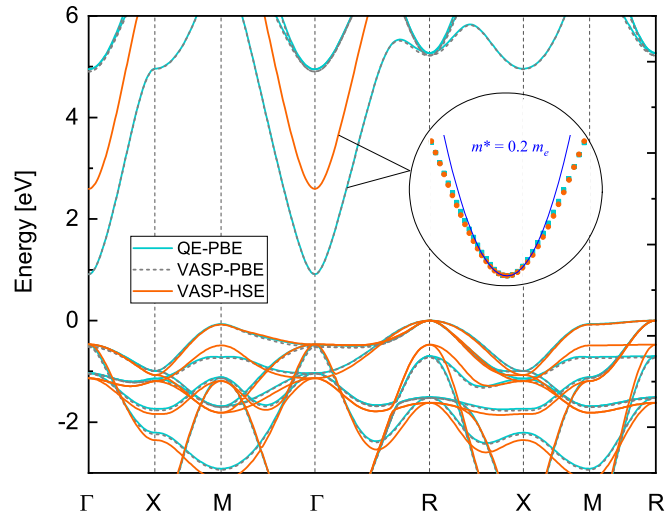

FIG. 2. Electronic band structure of $BaSnO_3$ calculated using QE and VASP with PBE and HSE exchange-correlation functionals. Inset shows the conduction band minimum of two band structures moved together and compared with the parabolic band structure with effective mass of $0.2m_e$.

the momentum relaxation time approximation (MRTA). The Hall mobility is calculated by

$$\boldsymbol{\mu}^H = \frac{2e}{n_c \Omega N_{\mathbf{k}}} \sum_{n\mathbf{k}} \mathbf{v}_{n\mathbf{k}} \mathbf{F}_{n\mathbf{k}}(\mathbf{B}) \left(-\frac{\partial f^0_{n\mathbf{k}}}{\partial \varepsilon_{n\mathbf{k}}} \right), \tag{6}$$

where $N_{\mathbf{k}}$ is the number of $\mathbf{k}$ grids and Ω is the volume of the unit cell. For $\mathbf{B} = 0$, Eq. (5) is reduced to the form of electronic transport under electric field, and Eq. (6) gives the drift mobility $\boldsymbol{\mu}$. The Hall mobility differs from the drift mobility by a Hall factor expressed as $\boldsymbol{\mu}^H = r\boldsymbol{\mu}$. If applying the magnetic field along the z direction, the Hall factor is [42]

$$r_{xy,z} = \sum_{\alpha\beta} \frac{\mu^{-1}_{x\alpha} \mu^H_{\alpha\beta,z} \mu^{-1}_{\beta,y}}{B_z}, \tag{7}$$

where x, y, α, β are the directions of the tensor matrix. For the cubic symmetric structure studied herein, the tensor has only one nondiagonal component which is independent of magnetic field.

III. RESULTS AND DISCUSSION

The phonon dispersion is calculated using VASP and PAW pseudopotentials with the PBE exchange-correlation functional, in which the $5s^2 5p^6 6s^2$ of Ba, $4d^{10} 5s^2 5p^2$ of Sn, and $2s^2 2p^4$ of O are taken as valence electrons. A $4 \times 4 \times 4$ supercell based on an experimental lattice constant of 4.12 Å [8,43] is built with Phonopy [44]. As plotted in Fig. 1, imaginary phonon modes exist around the R point. When the HSE is adopted, the imaginary frequencies are indeed removed, consistent with previous calculations [34]. More importantly, the frequencies of LO phonons calculated with HSE are 152, 410, and 726 cm^{-1}, in better agreement with experimental values of 154, 421, and 723 cm^{-1} especially for the second highest LO mode than those of PBE [32]. The long-range dipole-dipole interaction induced by polarization is included, which alters the phonon dispersion significantly, indicating the strong polar effect. The phonon dispersion calculated in QE with PBE is almost the same with that of VASP with PBE; therefore, it is reasonable to use the phonon dispersion obtained from VASP in the electronic transport calculations implemented in QE. The harmonic interatomic force constants are transformed from the VASP to QE format using an in-house code. The electronic state on $8 \times 8 \times 8$ $\mathbf{k}$ grids and perturbed potential on $4 \times 4 \times 4$ $\mathbf{q}$ grids are calculated in QE with PAW-modeled PBE pseudopotentials. The el-ph coupling matrix is constructed and interpolated using EPW [45] codes which are already built into QE.

The cubic $BaSnO_3$ is an indirect semiconductor, with the valence band maximum (VBM) located at the R point and the conduction band minimum (CBM) located at the zone center, as shown in Fig. 2. The band structure calculated with PBE using VASP is almost identical with that of QE. The calculated band gap is 0.91 eV, much smaller than the experimental value of 2.9–3.1 eV [46,47]. When the HSE is applied, the indirect band gap is opened up to 2.6 eV, which is still slightly underestimated but in good agreement with previous calculations [13,34,48]. The valence bands are much flatter than the conduction bands around the band extrema, suggesting poor hole transport properties of $BaSnO_3$. That is the reason that only the electron transport of $BaSnO_3$ is of concern in experimental and theoretical studies. To get different electron concentrations, the chemical potential level is manually shifted with respect to CBM [27,28]. The strong el-ph coupling probably induces the polaron effect, leading to the charge transport beyond the band paradigm. A representative perovskite oxide is strontium titanate ($SrTiO_3$), in which the presence of polarons is demonstrated and the electron mobility is significantly suppressed to about 5 cm^2 V^{-1} s^{-1} at room temperature [22]. But in strontium stannate ($SrSnO_3$) [49], which has phonon-limited electron mobility as high as 99 cm^2 V^{-1} s^{-1} at room temperature, the polaron effect is already weak enough to be neglected. Therefore, for the

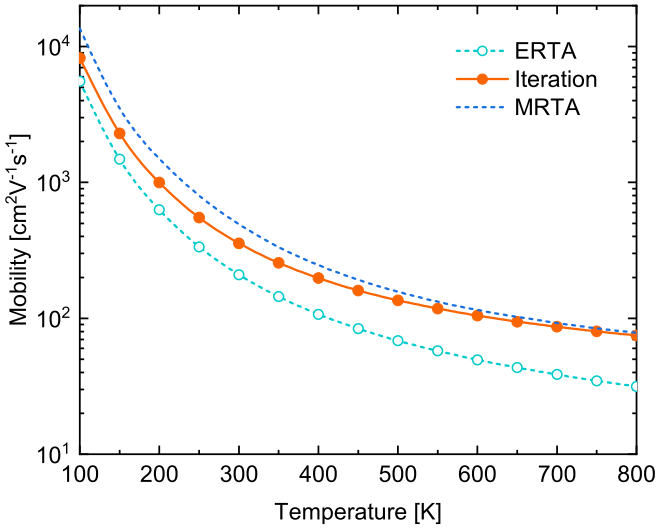

FIG. 3. Phonon-limited drift mobility at low carrier concentration limit as a function of temperature calculated with different solutions.

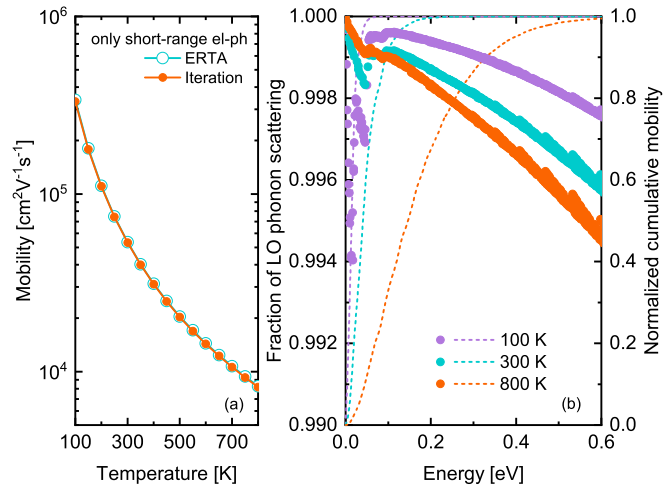

FIG. 4. (a) Drift mobility limited by short-range el-ph interactions. (b) Fraction of LO phonons scattering and the normalized cumulative mobility contributed by electrons at a given energy at different temperatures.

high-mobility $BaSnO_3$, the rigid-band approximation is used following the usual course of doping calculations. In this way, the transport calculations are not affected by the value of the band gap, but rely more on the band shape. The conduction bands with PBE are only slightly different from that of HSE, as shown in the inset of Fig. 2, where the conduction bands within 2 eV with respect to CBM are moved to the same vertex. Thus, the band structure of PBE is used herein although the band gap is underestimated. It is found that the valley around CBM is isotropic, and the fitted electron effective mass is about $0.2m_e$, in good agreement with previous calculations [12,13,48] and measurements at low carrier concentrations [50].

To calculate the electron mobility of $BaSnO_3$, the relevant properties involved in BTE are interpolated to fine $\mathbf{k}$ and $\mathbf{q}$ grids. It is noteworthy that the small effective mass makes that the Fermi level would easily go inside to the conduction bands at high carrier concentrations. In this situation, the electron states at high energy level need to be taken into account in the calculations. A threshold as large as 2.0 eV with respect to CBM is carefully examined and then used. The grid of fine $\mathbf{k}$ is set to be the same as that of $\mathbf{q}$, and a size of $128 \times 128 \times 128$ $\mathbf{k}$ and $\mathbf{q}$ points provides good convergence between 100 K and 800 K. Figure 3 shows the phonon-limited drift mobilities calculated within ERTA, MRTA, and iterative solutions of BTE under a low carrier concentration where the Fermi level is in the band gap. It is seen that the ERTA significantly underestimates the mobility, about 41% at room temperature. The underestimation increases monotonically from 32% at 100 K to 58% at 800 K. The mobility based on the MRTA, suggested for calculating electrical conductivity [51], is also given. The results are overestimated but the overestimation decreases with increasing temperature, which shows much better agreement with the exact solution than ERTA above room temperature. The calculated room-temperature drift mobilities are 209, 492, and 357 $cm^2\,V^{-1}\,s^{-1}$ with ERTA, MRTA, and the iterative solution of BTE, respectively.

The obvious underestimation of ERTA in polar materials has been noticed in previous studies [14,15], which is attributed to the LO phonon scattering for its divergent el-ph coupling around the zone center. Specifically, because of the rapid variation of the long-range el-ph coupling strengths, the scattering to different final states is strongly dependent on the direction of $\mathbf{q}$. The forward process involved in $W^{\mathbf{q}v}_{n\mathbf{k},m\mathbf{k}+\mathbf{q}}$ would be significantly different from the backward process and thus the summation term in Eq. (5) gives a considerable contribution. By contrast, for nonpolar scattering, the el-ph coupling strengths do not change dramatically. The forward process can be canceled out by the backward process and thus the summation term in Eq. (5) is negligible. This can be seen from the mobilities calculated by eliminating the long-range el-ph interactions in Fig. 4(a), which clearly shows that the ERTA gives similar results with those of iterative solution. Then, the increased underestimation of ERTA with increasing temperature can be understood by the enhanced contribution from LO phonon scattering, as shown in Fig. 4(b). The normalized cumulative distribution of mobility versus electron energy shows that the mobility is contributed by electrons with energy smaller than 0.05, 0.20, and 0.60 eV at 100, 300, and 800 K, respectively. In the contributing energy range, for 100 K, the fraction of LO phonon scattering is the lowest. Although there is a cross around 0.10 eV in the fraction distribution for 300 K and 800 K, about 90% mobility at 300 K is contributed by electrons with a smaller LO phonon scattering fraction than that of 800 K. Overall, as temperature increases, the contribution of LO phonon scattering is enhanced, leading to the enlarged underestimation by ERTA.

Figure 5 shows that the scattering rates by LO phonons are orders of magnitude higher than those of acoustic (TA+LA) and transverse optical (TO) phonons in a large energy range even up to 2 eV. The polar contribution in $BaSnO_3$ is much greater than that of the most famous strongly polar material GaAs [15], leading to the unprecedentedly large underestimation of ERTA in $BaSnO_3$. The electron mobility at low temperatures is ultrahigh, reaching up to 8228 $cm^2\,V^{-1}\,s^{-1}$ at

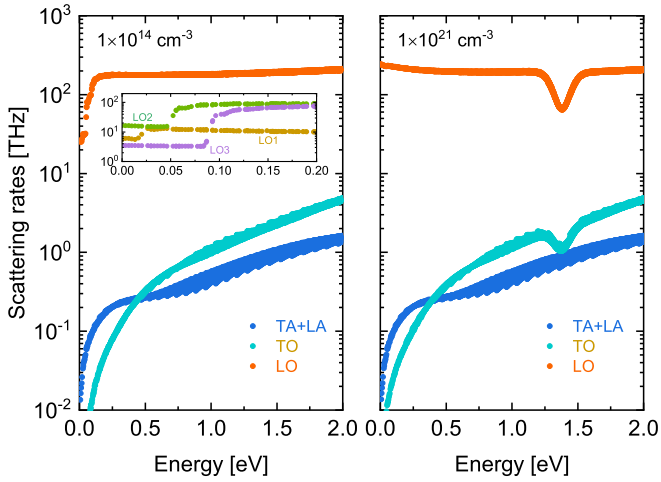

FIG. 5. Room-temperature el-ph scattering rates contributed from TA+LA, TO, LO phonons at different carrier concentrations, where the inset shows the scattering rates of three LO phonon modes.

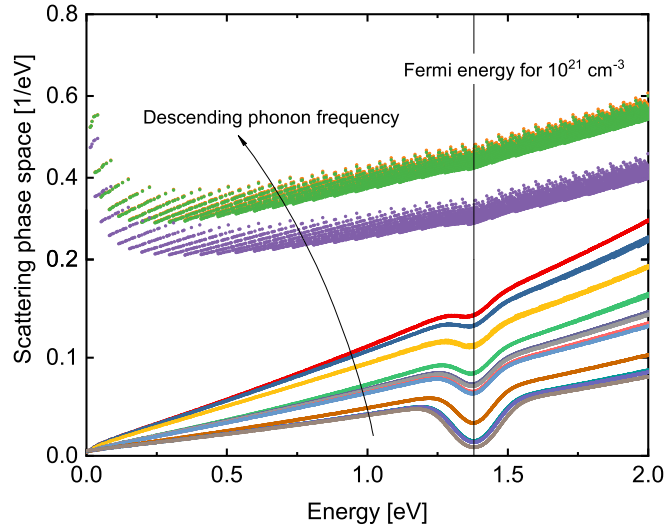

FIG. 6. Scattering phase space for different phonon modes ordered by the phonon frequencies at electron concentration of 10^{21} cm^{-3}.

100 K, whereas it decreases quickly down to 75 cm^2 V^{-1} s^{-1} as temperature increases to 800 K. The avalanche of reduction is attributed to the two-plateau energy dependence of LO phonon scattering rates, as shown in the inset of Fig. 5. The sudden increase of LO phonon scattering appears at the energy close to its phonon frequency, namely, 0.02, 0.05, and 0.09 eV, respectively, due to the occurrence of LO phonon emission processes [14,15,52]. The low-energy plateau of scattering rates corresponds to the LO phonon absorption processes. The thermally activated scattering rates for absorption and emission processes are proportional to the LO phonon occupation as $n_{\mathbf{q}\nu}$ and $1 + n_{\mathbf{q}\nu}$, respectively [22,52]. The $(1 + n_{\mathbf{q}\nu})/n_{\mathbf{q}\nu}$ values for the LO1, LO2, and LO3 modes are about 2.1, 7.1, and 32.5 at room temperature. As temperature increases, the absorption scattering increases enormously; meanwhile the contribution from high-energy electrons is enlarged so that the emission scattering plays an increasingly important role. The temperature-induced great enhancement of LO phonon scattering gives rise to the rapid reduction in electron mobility.

It is interesting that the dominance of LO phonon scattering is retained in heavily doped systems even at 1×10^{21} cm^{-3}, as shown in Fig. 5. There is a dip around 1.4 eV, corresponding to the Fermi energy of 1×10^{21} cm^{-3} carrier concentration, in the scattering rates of TO and LO phonons but not the TA and LA phonons. This is a consequence of the factor in the square brackets of Eq. (2) that determines the absorption and emission processes involving a phonon, which can be called a scattering phase space. For optical phonons, $n_{\mathbf{q}p}$ is close to constant due to its nearly invariant frequency since the relevant phonons are constrained around the zone center by the momentum conservation with electrons. The scattering phase space is mainly determined by the electron distribution function $f_{m\mathbf{k}+\mathbf{q}}$ and $1 - f_{m\mathbf{k}+\mathbf{q}}$ corresponding to absorbing and emitting a phonon, respectively. For an initial state located at the Fermi level, the factor is the lowest, whereas for an initial state above and below the Fermi level, the factor becomes larger [13]. Considering a positive contribution of $n_{\mathbf{q}p}$, which is inversely proportional to phonon frequency, the dip becomes smaller as the phonon frequency decreases, as shown in Fig. 6. For acoustic phonons, the phonon frequency is much smaller as compared to optical phonons, which probably gives a considerable compensation that results in the disappearance of the dip in the scattering phase spaces and scattering rates.

The Hall factor at low carrier concentration limit increases from 1.06 at 100 K to 1.17 at 300 K and then deceases to 1.03 at 800 K, while the ERTA has an overestimation of about 8%–13%, as shown in Fig. 7. For comparison, the values calculated from the popularly used formula of $r^{iso} = \langle\tau^2\rangle/\langle\tau\rangle^2$ are given, which is based on the isotropic parabolic assumption and $\langle\tau\rangle$ denotes the energy-weighted average of relaxation time. There is distinct deviation from the exact values, but the trend is roughly similar and thus it can qualitatively analyze the temperature dependence to some

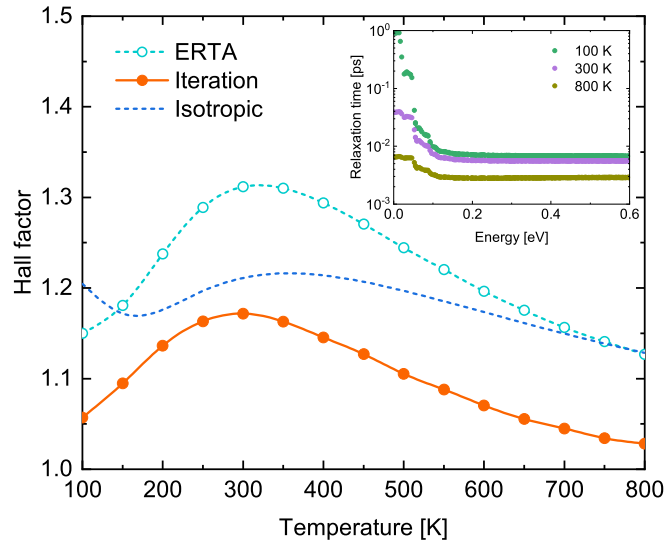

FIG. 7. Phonon-limited Hall factor at low carrier concentration limit as a function of temperature calculated with different solutions.

extent. If particularly describing the energy dependence of the relaxation time by a power law $\tau \propto \varepsilon^{-d}$, r^{iso} has an especially simple form as [53] $r^{iso} = \Gamma(\frac{5}{2} - 2d)\Gamma(\frac{5}{2})/[\Gamma(\frac{5}{2} - d)]^2$ where $\Gamma(x)$ is the gamma function. It is mathematically easy to prove that $\langle\tau^2\rangle/\langle\tau\rangle^2$ is always greater than 1. The simple expression is an upward concave function of d; for instance, the d of $-1/2$ (acoustic piezoelectric scattering) and 0 and $1/2$ (acoustic deformation potential scattering and nonpolar optical phonon scattering) yields r^{iso} of 1.10, 1.00, and 1.18, respectively. Because of the dominance of LO phonon scattering, the energy dependencies of relaxation times for $BaSnO_3$ at different temperatures have similar shape, as shown in the inset of Fig. 7, which drops stepwise below 0.1 eV due to the occurrence of LO phonon emission processes at three different frequencies and then remains almost constant above 0.1 eV. As temperature increases, the damping of relaxation time becomes smaller; thus the r^{iso} has a reduction. However, it should be said that the dependence cannot be fully explained, even for the simplified r^{iso}, let alone the real values that are significantly different even for homologous semiconductors [42].

Previous calculations based on semiempirical approximations in Ref. [13] reported that the ionized impurity scattering significantly affects the mobility even at room temperature, with a reduction of 50% at 1×10^{20} cm^{-3} doping density. Therefore, the ionized impurity scattering is considered using the Brooks and Herring model, as [54,55]

$$\tau_{n\mathbf{k}}^{-1} = \frac{2\pi Z^2 n_I e^4}{\hbar\Omega(\epsilon_r\epsilon_0)^2}\frac{1}{N_{\mathbf{k}}}\sum_{m\mathbf{k}'}\frac{\delta(\varepsilon_{m\mathbf{k}'} - \varepsilon_{n\mathbf{k}})}{\left(\beta_s^2 + |\mathbf{k}' - \mathbf{k}|^2\right)^2}, \tag{8}$$

where Z is the number of free carriers given by an impurity atom and n_I is the impurity density. Considering La atom doping and assuming full ionization, Z is set to 1 and n_I is equal to the carrier concentration. $\epsilon_r\epsilon_0$ is the static dielectric constant; β_s is the screening length defined by Thomas-Fermi theory as [54,55]

$$\beta_s^2 = \frac{n_I e^2}{\epsilon_r\epsilon_0 k_B T}. \tag{9}$$

As shown in Fig. 8, the impurity scattering decreases the mobility, with the largest reduction only about 25% appearing around 5×10^{17} cm^{-3}. As concentration increases, the effect of impurity scattering is weakened and only about 5% reduction at 1×10^{20} cm^{-3}. The corresponding impurity scattering rates are also orders of magnitude smaller than phonon scattering rates. The influence of ionized impurity is much weaker than the prediction in Ref. [13]. It is noticed that the isotropic parabolic assumption was used in Ref. [13]; then the model is rewritten as [13,49]

$$\tau_{n\mathbf{k}}^{-1} = \frac{n_I Z^2 e^4}{16\pi(\epsilon_r\epsilon_0)^2(2m^*)^{1/2}}\varepsilon_{n\mathbf{k}}^{-3/2} \times\left[\ln\left(1 + \frac{8m^*\varepsilon_{n\mathbf{k}}}{\hbar^2\beta_s^2}\right) - \left(1 + \frac{\hbar^2\beta_s^2}{8m^*\varepsilon_{n\mathbf{k}}}\right)^{-1}\right], \tag{10}$$

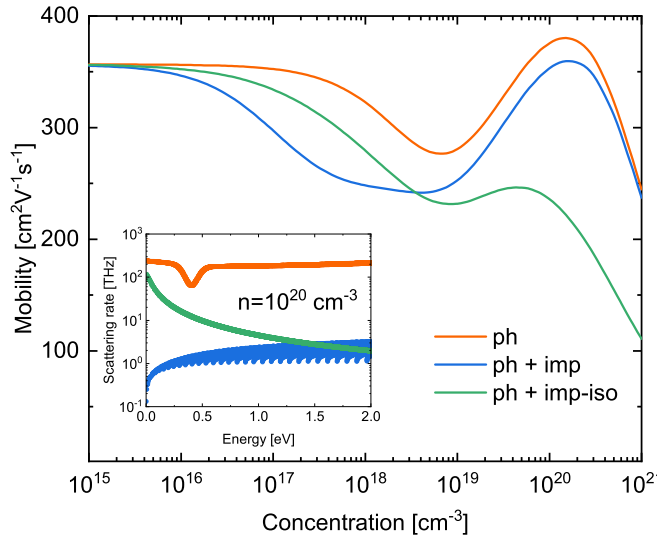

FIG. 8. Drift mobility limited by phonons (ph) as a function of carrier concentration at room temperature and that additionally considering the impurity scattering using full band structure (imp) and isotropic single parabolic assumption (imp-iso). The inset gives the corresponding phonon and impurity scattering rates at a concentration of 10^{20} cm^{-3}.

where m^* is the electron effective mass, and the screening vector β_s becomes [13,49]

$$\beta_s^2 = \frac{2^{1/2}m^{*3/2}e^2}{\pi^2\hbar^3\epsilon_r\epsilon_0}\int_0^\infty \varepsilon^{1/2}\left(-\frac{\partial f}{\partial\varepsilon}\right)d\varepsilon. \tag{11}$$

The resulting impurity scattering rates under isotropic parabolic assumption are greater than that without this assumption. The calculated mobilities are obviously decreased especially at high concentrations, by about 38% at the concentration of 1×10^{20} cm^{-3}, which is close to the conclusion of Ref. [13]. The results obtained by the two simplified models differ so much that the role of impurity scattering in $BaSnO_3$ remains somewhat uncertain. The recently developed *ab initio* approaches for electron-defect scattering including neutral and ionized impurities [56,57] require no prior assumptions and can therefore be used for further clarification. The negligible effect of impurity scattering is also found in the high-mobility $SrSnO_3$ above room temperature, where the mobility is limited by phonons and thus is nearly independent of carrier concentration [49].

The calculated room-temperature resistivity and mobility at different carrier concentrations are compared with experiments in Figs. 9(a) and 9(b). As expected, the phonon-limited resistivity is smaller than the experimental values and the Hall mobility is larger than the experimental values. Below the concentration of 1×10^{17} cm^{-3}, the chemical potential is located in the band gap and the mobility is independent of carrier concentration. As concentration increases, the chemical potential would move inside the conduction bands. The mobility decreases first due to the increased contribution from high-energy electrons which are subjected to stronger phonon scattering. Afterward, because of the reduction of scattering around Fermi energy, as shown in Fig. 5, the mobility has an increase and then decreases again. The upper limits of drift

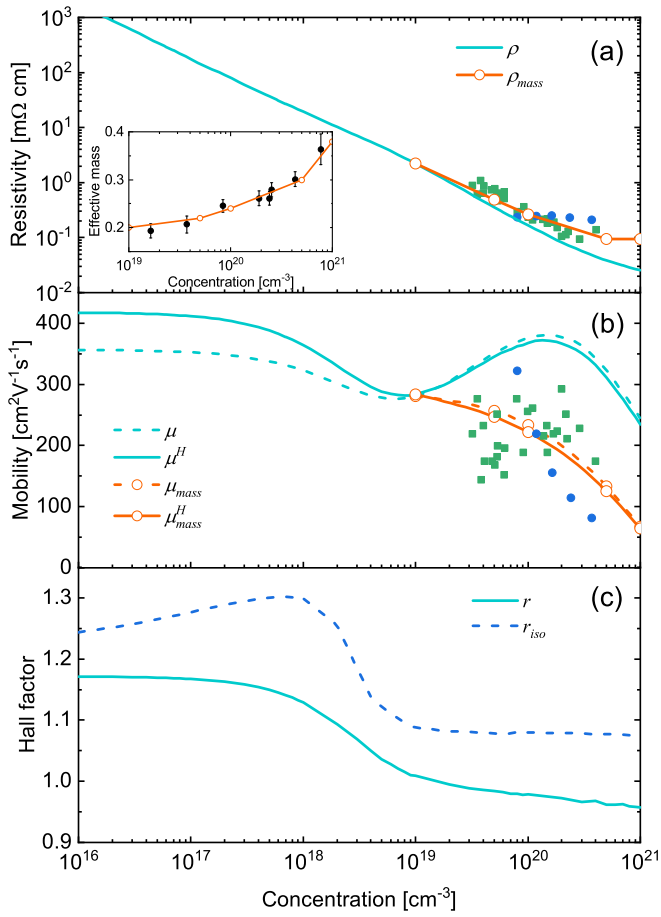

FIG. 9. Phonon-limited (a) resistivity, (b) drift and Hall mobility, (c) Hall factor as a function of carrier concentration at room temperature as compared with experimental values from Ref. [50] (green square) and Ref. [8] (blue circle). Inset in (a) shows the renormalized effective mass at different concentration as compared with experimental values from Ref. [50]. The subscript *mass* corresponds to the calculated results with the renormalized band structure.

and Hall mobilities in doped systems are 377 $cm^2\,V^{-1}\,s^{-1}$ and 367 $cm^2\,V^{-1}\,s^{-1}$ at a concentration of 2×10^{20} cm^{-3}, respectively. It is noteworthy that the measured resistivity and mobility are very dispersive although the samples come from the same batch [8,9]. Besides the tentatively presumed sample-dependent defects [9], the remarkably increased electron effective mass in the high-doping regime [50] is worth discussing since the effective mass can significantly alter the transport properties [15]. To reproduce the experimental effective mass, which increases with increasing carrier concentration, the band structure within the energy threshold is simply changed with electron energy and velocity at a given wave vector scaled by different constant factors since only the single-band valley participates in the transport. This yields an effective mass of 0.22, 0.24, 0.30, and 0.38 m_e at 5×10^{19}, 1×10^{20}, 5×10^{20}, and 1×10^{21} cm^{-3}, respectively, which can reasonably agree with the experimentally measured effective mass as plotted in the inset of Fig. 9(a). As compared to the results with raw band structure, the calculated resistivity increases while the mobility decreases significantly as expected. Moreover, the calculated results pass through the central region of the dispersive experimental values. In addition, it is found that the Hall factor is dependent on carrier concentration and decreases with increasing concentration, from 1.17 at 1×10^{16} cm^{-3} to 0.96 at 1×10^{21} cm^{-3}, as shown in Fig. 9(c). The Hall factor can be smaller than 1 whereas the formula based on isotropic parabolic assumption is invalid at this point because it cannot give a Hall factor smaller than unity. The large deviation indicates that the accurate solution based on *ab initio* BTE is necessary for the carrier transport in the presence of magnetic field.

IV. CONCLUSION

In summary, the drift and Hall mobilities of cubic $BaSnO_3$ are calculated using an exact *ab initio* approach with iterative solution of linearized BTE in the presence of electric and magnetic fields. The Hall factor is found to be dependent on temperature and carrier concentration, which can be smaller or larger than unity, whereas the usually used formula based on the isotropic parabolic assumption leads to obvious overestimation and cannot be less than 1 mathematically. At room temperature, the Hall factor decreases from 1.17 at 1×10^{16} cm^{-3} to 0.96 at 1×10^{21} cm^{-3} in the phonon-limited intrinsic system. The scattering rates decoupled by different phonon modes show that the polar scattering by LO phonons can be orders of magnitude larger than that of other phonons. This strongly dominant role of LO phonon scattering can be retained for high-energy electrons and thus for high carrier concentration situations. As a result, the energy relaxation time approximation of BTE would significantly underestimate the mobility, as large as 32% at 100 K and increasing to 58% at 800 K under the low-concentration limit, while the momentum relaxation time approximation has good agreement above room temperature. The increased underestimation is attributed to the enlarged contribution of LO phonon scattering. The ionized impurity scattering in doping systems is much smaller than phonon scattering, whereas the enlarged effective mass can significantly reduce the mobility; thus the effective mass altered by doping is more likely to be one of the causes of irregularly dispersed measured values.

ACKNOWLEDGMENTS

J.M. acknowledges support from the National Natural Science Foundation of China (Grant No. 11804229). W.L. was supported by the Guangdong Basic and Applied Basic Research Foundation (Grant No. 2021A1515010042) and the Stable Support Plan of the Higher Education Institutions of Shenzhen (Grant No. 20200809161605001).

[1] S. H. Wemple, M. DiDomenico, and A. Jayaraman, Phys. Rev. **180**, 547 (1969).

[2] H. P. R. Frederikse, W. R. Thurber, and W. R. Hosler, Phys. Rev. **134**, A442 (1964).

[3] K. Ueda, H. Yanagi, H. Hosono, and H. Kawazoe, Phys. Rev. B **56**, 12998 (1997).

[4] T. Kolodiazhnyi, A. Petric, M. Niewczas, C. Bridges, A. Safa-Sefat, and J. E. Greedan, Phys. Rev. B **68**, 085205 (2003).

[5] H. F. Wang, Q. Z. Liu, F. Chen, G. Y. Gao, W. Wu, and X. H. Chen, J. Appl. Phys. **101**, 106105 (2007).

[6] Q. Liu, J. Dai, Z. Liu, X. Zhang, G. Zhu, and G. Ding, J. Phys. D: Appl. Phys. **43**, 455401 (2010).

[7] X. Luo, Y. S. Oh, A. Sirenko, P. Gao, T. A. Tyson, K. Char, and S.-W. Cheong, Appl. Phys. Lett. **100**, 172112 (2012).

[8] H. J. Kim, U. Kim, H. M. Kim, T. H. Kim, H. S. Mun, J. Kim, B. G. Jeon, K. T. Hong, W. J. Lee, and C. Ju, Appl. Phys. Express **5**, 061102 (2012).

[9] H. J. Kim, U. Kim, T. H. Kim, J. Kim, H. M. Kim, B.-G. Jeon, W.-J. Lee, H. S. Mun, K. T. Hong, J. Yu, K. Char, and K. H. Kim, Phys. Rev. B **86**, 165205 (2012).

[10] H. Toyosaki, M. Kawasaki, and Y. Tokura, Appl. Phys. Lett. **93**, 132109 (2008).

[11] T. Kamiya and H. Hosono, NPG Asia Mater. **2**, 15 (2010).

[12] H.-R. Liu, J.-H. Yang, H. J. Xiang, X. G. Gong, and S.-H. Wei, Appl. Phys. Lett. **102**, 112109 (2013).

[13] K. Krishnaswamy, B. Himmetoglu, Y. Kang, A. Janotti, and C. G. Van de Walle, Phys. Rev. B **95**, 205202 (2017).

[14] T.-H. Liu, J. Zhou, B. Liao, D. J. Singh, and G. Chen, Phys. Rev. B **95**, 075206 (2017).

[15] J. Ma, A. S. Nissimagoudar, and W. Li, Phys. Rev. B **97**, 045201 (2018).

[16] S. Poncé, W. Li, S. Reichardt, and F. Giustino, Rep. Prog. Phys. **83**, 036501 (2020).

[17] W. Li, Phys. Rev. B **92**, 075405 (2015).

[18] F. Giustino, M. L. Cohen, and S. G. Louie, Phys. Rev. B **76**, 165108 (2007).

[19] C. Verdi and F. Giustino, Phys. Rev. Lett. **115**, 176401 (2015).

[20] J. Sjakste, N. Vast, M. Calandra, and F. Mauri, Phys. Rev. B **92**, 054307 (2015).

[21] Q. Song, T.-H. Liu, J. Zhou, Z. Ding, and G. Chen, Mater. Today Phys. **2**, 69 (2017).

[22] J.-J. Zhou, O. Hellman, and M. Bernardi, Phys. Rev. Lett. **121**, 226603 (2018).

[23] J.-J. Zhou and M. Bernardi, Phys. Rev. B **94**, 201201(R) (2016).

[24] J. Ma, Y. Chen, and W. Li, Phys. Rev. B **97**, 205207 (2018).

[25] T.-H. Liu, B. Song, L. Meroueh, Z. Ding, Q. Song, J. Zhou, M. Li, and G. Chen, Phys. Rev. B **98**, 081203(R) (2018).

[26] S. Poncé, D. Jena, and F. Giustino, Phys. Rev. B **100**, 085204 (2019).

[27] J. Ma, F. Meng, D. Xu, R. Hu, and X. Luo, J. Phys.: Condens. Matter **32**, 465704 (2020).

[28] J. Ma, A. S. Nissimagoudar, S. Wang, and W. Li, Phys. Status Solidi RRL **14**, 2000084 (2020).

[29] P. Giannozzi Jr., O. Andreussi, T. Brumme, O. Bunau, M. B. Nardelli, M. Calandra, R. Car, C. Cavazzoni, D. Ceresoli, M. Cococcioni, N. Colonna, I. Carnimeo, A. D. Corso, S. de Gironcoli, P. Delugas, R. A. DiStasio, A. Ferretti, A. Floris, G. Fratesi, G. Fugallo *et al.*, J. Phys.: Condens. Matter **29**, 465901 (2017).

[30] P. V. Balachandran, D. Xue, and T. Lookman, Phys. Rev. B **93**, 144111 (2016).

[31] L. Chen, Y. Zhang, X. Wang, B. Jalan, S. Chen, and Y. Hou, J. Phys. Chem. C **122**, 11482 (2018).

[32] T. N. Stanislavchuk, A. A. Sirenko, A. P. Litvinchuk, X. Luo, and S.-W. Cheong, J. Appl. Phys. **112**, 044108 (2012).

[33] E. Bévillon, A. Chesnaud, Y. Z. Wang, G. Dezanneau, and G. Geneste, J. Phys.: Condens. Matter **20**, 145217 (2008).

[34] B. Monserrat, C. E. Dreyer, and K. M. Rabe, Phys. Rev. B **97**, 104310 (2018).

[35] J. Li, Z. Ma, R. Sa, and K. Wu, RSC Adv. **7**, 32703 (2017).

[36] F. Szmulowicz, Phys. Rev. B **28**, 5943 (1983).

[37] F. Szmulowicz and F. L. Madarasz, Phys. Rev. B **27**, 2605 (1983).

[38] F. Szmulowicz and F. L. Madarasz, Phys. Rev. B **27**, 6279 (1983).

[39] F. Szmulowicz, Phys. Rev. B **34**, 4031 (1986).

[40] F. Macheda and N. Bonini, Phys. Rev. B **98**, 201201(R) (2018).

[41] D. C. Desai, B. Zviazhynski, J.-J. Zhou, and M. Bernardi, Phys. Rev. B **103**, L161103 (2021).

[42] S. Poncé, F. Macheda, E. R. Margine, N. Marzari, N. Bonini, and F. Giustino, Phys. Rev. Res. **3**, 043022 (2021).

[43] H. J. Kim, J. Kim, T. H. Kim, W.-J. Lee, B.-G. Jeon, J.-Y. Park, W. S. Choi, D. W. Jeong, S. H. Lee, J. Yu, T. W. Noh, and K. H. Kim, Phys. Rev. B **88**, 125204 (2013).

[44] A. Togo and I. Tanaka, Scr. Mater. **108**, 1 (2015).

[45] S. Poncé, E. Margine, C. Verdi, and F. Giustino, Comput. Phys. Commun. **209**, 116 (2016).

[46] H. Mizoguchi, H. W. Eng, and P. M. Woodward, Inorg. Chem. **43**, 1667 (2004).

[47] S. A. Chambers, T. C. Kaspar, A. Prakash, G. Haugstad, and B. Jalan, Appl. Phys. Lett. **108**, 152104 (2016).

[48] D. O. Scanlon, Phys. Rev. B **87**, 161201(R) (2013).

[49] T. K. Truttmann, J.-J. Zhou, I.-T. Lu, A. K. Rajapitamahuni, F. Liu, T. E. Mates, M. Bernardi, and B. Jalan, Commun. Phys. **4**, 241 (2021).

[50] C. A. Niedermeier, S. Rhode, K. Ide, H. Hiramatsu, H. Hosono, T. Kamiya, and M. A. Moram, Phys. Rev. B **95**, 161202(R) (2017).

[51] S. Li, Z. Tong, X. Zhang, and H. Bao, Phys. Rev. B **102**, 174306 (2020).

[52] F. Meng, J. Ma, J. He, and W. Li, Phys. Rev. B **99**, 045201 (2019).

[53] D. A. Anderson and N. Apsley, Semicond. Sci. Technol. **1**, 187 (1986).

[54] D. Chattopadhyay and H. J. Queisser, Rev. Mod. Phys. **53**, 745 (1981).

[55] M. Fiorentini and N. Bonini, Phys. Rev. B **94**, 085204 (2016).

[56] I.-T. Lu, J.-J. Zhou, and M. Bernardi, Phys. Rev. Mater. **3**, 033804 (2019).

[57] I.-T. Lu, J.-J. Zhou, J. Park, and M. Bernardi, Phys. Rev. Mater. **6**, L010801 (2022).